Computers & Fluids 47 (2011) 85–100

Contents lists available at ScienceDirect

Computers & Fluids

journal homepage: www.elsevier.com/locate/compfluid

Direct numerical simulation of compressible turbulent channel flows using the discontinuous Galerkin method

Liang Wei, Andrew Pollard *

Department of Mechanical and Materials Engineering, Queen's University, Kingston, Ontario, Canada K7L 3N6

ARTICLE INFO

Article history:
Received 21 January 2010
Received in revised form 30 January 2011
Accepted 22 February 2011
Available online 5 March 2011

Keywords:
Direct numerical simulation
Discontinuous Galerkin method
Turbulent channel flow
Compressible flow
Mach number
Turbulence structures

ABSTRACT

Direct numerical simulation of turbulent channel flows between isothermal walls have been carried out using discontinuous Galerkin method. Three Mach numbers are considered (0.2, 0.7, and 1.5) at a fixed Reynolds number ≈2800, based on the bulk velocity, bulk density, half channel width, and dynamic viscosity at the wall. Power law and log-law with the scaling of the mean streamwise velocity are considered to study their performance on compressible flows and their dependence on Mach numbers. It indicates that power law seems slightly better and less dependent on Mach number than the log-law in the overlap region. Mach number effects on the second-order (velocity, pressure, density, temperature, shear stress, and vorticity fluctuations) and higher-order (skewness and flatness of velocity, pressure, density, and temperature fluctuations) statistics are explored and discussed. Both inner (that is wall variables) and outer (that is global) scalings (with Mach number) are considered. It is found that for some second-order statistics (i.e. velocity, density, and temperature), the outer scaling collapses better than the inner scaling. It is also found that near-wall large-scale motions are affected by Mach number. The near-wall spanwise streak spacing increases with increasing Mach number. Iso-surfaces of the second invariant of the velocity gradient tensor are more sparsely distributed and elongated as Mach number increases, which is similar to the distribution of near-wall low speed streaks.

1. Introduction

Wall bounded turbulent flows are important because they are wildly used in practical engineering applications, such as the external flow around airplanes, ships, and buildings, the internal flow through turbine blades, pipes, and channels. It has been demonstrated that incompressible turbulent channel flow is extremely useful for the study of wall-bounded turbulence [17]. Direct numerical simulation (DNS) of wall-bounded compressible turbulent flow is equally useful because it provides 3D and time-dependent data that are very difficult or even impossible to obtain experimentally [19]. These earlier investigators used spectral, finite volume-type solvers; here, the discontinuous Galerkin method (DGM) is used for the DNS to assess the method and to study the effects of Mach number and compressibility effects on turbulence statistics, turbulence structures, and related turbulence physics.

DGM is a finite element based method that uses numerical fluxes on element boundaries, which draws from the finite volume method, so that it can accommodate discontinuous solutions on element boundaries. It has many attractive features including: high order accuracy, highly parallelizable, well suited for complex geometries, local conservation, etc. [6]. The first DGM was introduced by Reed and Hill [25]. It is only recently that DGM has been made suitable for computational fluid dynamics related applications [6,14], see [33] for details. The first application of DGM to DNS of turbulent flows was performed by [9], who applied the DGM to a low-Reynolds-number DNS of compressible turbulent channel flow with isothermal walls. The Reynolds number based on the friction velocity (Re_τ) was 100. The center-line Mach number (Ma_c) was 0.3. Mean and RMS velocity profiles were obtained and compared with the incompressible cases. To the best of the author's knowledge, this is the only application of DGM to DNS of turbulent flows.

There are two types of compressibility effects. One is caused by variations of the mean properties such as density and viscosity, and the other the fluctuation of thermodynamic quantities [19]. Lele [16] has reviewed compressibility effects on turbulence. He summarized many facets of compressibility effects on turbulence and discussed several homogeneous and inhomogeneous compressible flows. He argued that the density gradient in a compressible turbulent boundary layer is mainly responsible for a decreased skin-friction coefficient, smaller turbulence intensity, viscous effects, and for modifications to the incompressible law of the wall. Smits [29] also argued that a single Reynolds number is not sufficient to characterize the flow with large gradients of fluid properties.

* Corresponding author.
E-mail address: pollard@me.queensu.ca (A. Pollard).

0045-7930/$ - see front matter © 2011 Elsevier Ltd. All rights reserved.
doi:10.1016/j.compfluid.2011.02.015

Nomenclature

CKM	Coleman, Kim, and Moser [8]
DGM	Discontinuous Galerkin method
DNS	Direct Numerical Simulation
KMM	Kim, Moin, and Moser [15]
MKM	Moser, Kim, and Mansour [23]
RMS	Root-Mean-Square
TKE	Turbulent Kinetic Energy
A	Jacobian matrix
A_k	Advection term
c_p	Specific heat for constant pressure
c_v	Specific heat for constant volume
C_k	Compressibility term
D_k	Diffusion term
$\mathbf{D}$	Diagonal matrix of the eigenvalues
E	Total energy per unit volume
F	Flatness factor
$\mathbf{F}_B$	Body force terms
$\mathbf{F}^I$	Inviscid flux
$\mathbf{F}^V$	Viscous flux
$\widehat{\mathbf{F}}^I$	Numerical boundary flux for convection
$\widehat{\mathbf{f}}^V$	Numerical boundary flux for diffusion
h	Half channel width
k	Turbulence kinetic energy
$\mathbf{L}$	Left eigenvector
Ma	Mach number
p	Pressure
P_k	Production term
P	Polynomial order Negative dilatation $-\partial u_i/\partial x_i$
Q	Second invariant of the velocity gradient tensor
R	Specific gas constant
$\mathbf{R}$	Right eigenvector
Re	Reynolds number
Re_τ	Friction Reynolds number $\rho u_\tau h/\mu$
R_{ij}	$0.5(\partial u_i/\partial x_j - \partial u_j/\partial x_i)$
S_{ij}	$0.5(\partial u_i/\partial x_j + \partial u_j/\partial x_i)$
S	Skewness factor
s	Source term
T	Temperature
t	Time
$\mathbf{U}$	Variables $[\rho, \rho u, \rho v, \rho w, E]^t$
U_m	Mean bulk velocity
U_+	External value at element boundary
U_-	Internal value at element boundary
u^+	$u^+ = u/u_\tau$
u_τ	Friction velocity
$\mathbf{W}$	Weighting function
y^+	$y^+ = y/(\nu/u_\tau)$
β	Power law coefficient
δ_{ij}	Kronecker delta
δ_ν	Viscous length scale ν/u_τ
ϵ_k	Dissipation term
γ	Log-law coefficient Ratio of specific heats c_p/c_v
κ	Thermal conductivity Von Kármán constant
μ	Dynamic viscosity
μ_{ref}	Reference dynamic viscosity
ν	Kinematic viscosity Variable coefficient
Ω	The whole computational domain
ω	Vorticity
ω_x	Streamwise vorticity
ω_y	Wall normal vorticity
ω_z	Spanwise vorticity
Ω^e	The e-th element
$\partial\Omega$	The boundary of the domain
ρ	Density
τ, τ_{ij}	Shear stress
$\tau_{w_{av}}$	Shear stress averaged on both walls
$\langle\rangle$	Reynolds average, i.e. $\langle\phi\rangle$
$\{\}$	Favre average $\{\phi\} = \langle\rho\phi\rangle/\langle\rho\rangle$
$()'$	Fluctuation $\phi' = \phi - \langle\phi\rangle$
$()''$	Favre fluctuation $\phi'' = \phi - \{\phi\}$
$()^*$	Nondimensionalized variable
$()_{\mathrm{m}}$	Bulk Variable
$()_{rms}$	RMS of a quantity
$()_t$	Time derivative of a variable
$()_{\mathrm{w}}$	Variable value at the wall

The first DNS of incompressible turbulent plane channel flow was performed by Kim et al. [15], referred to hereafter as KMM. The Reynolds number based on friction velocity was around 180 ($Re_\tau \approx 180$). A large number of turbulence statistics including turbulence intensities, Reynolds shear stress, vorticity, high order statistics, etc., were compared with experimental data with good agreement.

New simulations of the KMM $Re_\tau \approx 180$ case were performed by Moser et al. [23], referred to hereafter as MKM. A comprehensive database was provided including mean profiles, Reynolds stress, skewness, and flatness profiles, etc. Besides this, two higher Reynolds number ($Re_\tau \approx 395$ and $Re_\tau \approx 590$) for fully developed turbulent channel flow simulations were conducted [23], in which fewer low Reynolds number effects were observed than the $Re_\tau \approx 180$ case. For example, near-wall scaling of mean streamwise velocity profile for the case $Re_\tau \approx 180$ has a larger intercept in the log-law region than for higher Reynolds number flows.

DNS of turbulent compressible plane channel flow between isothermal walls was performed by Coleman et al. [8]. The Mach numbers based on the bulk velocity and sound speed at the walls were 1.5 (referred to henceforth as CKM) and 3. The Reynolds numbers were 3000 ($Re_\tau = 222$) and 4880 ($Re_\tau = 451$) respectively, based on the bulk velocity and channel half-width. They found that the mean density and temperature gradients caused enhanced streamwise coherence of near-wall streaks. The density-weighted Van Driest transformation [31] of mean streamwise velocity generated curves with similar slopes. It was also claimed that the compressibility effects caused by the mean property variations were dominant, compared with those caused by thermodynamic fluctuations.

Huang et al. [13] analyzed the DNS results of fully developed supersonic isothermal wall channel flow and found that the difference between Reynolds and Favre averages was small and any difference mainly existed in the region close to the wall. Their DNS results did not support the "strong Reynolds analogy" that links temperature and streamwise velocity fluctuations, as proposed by Morkovin [20]. Instead, they proposed a new Reynolds analogy that had good agreement with their DNS data.

Morinishi et al. [19] performed a DNS of a compressible turbulent channel flow between adiabatic and isothermal walls. The main difference between the results obtained when adiabatic and isothermal walls were employed was explained. The energy transfer was analyzed. It was found that Morkovin's hypothesis [20], which generally claimed that the compressible shear flow dynamics should follow what is observed in incompressible flow, was not applicable to the near-wall asymptotic behavior of the wall-normal turbulence intensity.

Foysi et al. [10] used DNS to study Reynolds shear stress scaling in turbulent supersonic channel flow with isothermal walls. It was found that the outer scaling (scaling with global variables) of Reynolds stresses worked well in the region far away from the wall, but inner scaling (scaling with wall variables) failed. An effective density was proposed based on an integral of local mean density over the vertical extent of a turbulent eddy. They claimed that the local-mean-density-based turbulence inner scaling law failed because of the difference between the effective and local mean density.

In this paper the effects of Mach number on compressible channel flow are explored with reference to mean profiles, second-order and higher-order statistics of velocity and thermodynamic properties as well as the turbulent kinetic energy budget and their dependence on inner/outer scaling variables. The near-wall turbulence structures educed using the "Q" criteria are also considered.

2. Computational details

2.1. Numerical methods

DNS of fully developed turbulent flow between two isothermal parallel plates at different Mach numbers is considered. The fluid is assumed to be an ideal gas with constant specific heats ($c_p = \gamma R/(\gamma-1)$, $c_v = R/(\gamma-1)$; $\gamma = 1.4$, R is the gas constant) and Prandtl number (Pr).

The nondimensionalized conservative form of continuity, momentum, and energy equations with an addition of a driving force can be written as:

$$\frac{\partial\rho^*}{\partial t^*}+\frac{\partial\rho^* u_j^*}{\partial x_j^*}=0, \tag{1}$$

$$\frac{\partial\rho^* u_i^*}{\partial t^*}+\frac{\partial\left(\rho^* u_i^* u_j^*+p^*\delta_{ij}\right)}{\partial x_j^*}=\frac{1}{Re}\frac{\partial\tau_{ij}^*}{\partial x_j^*}+\rho^* f_i^*, \tag{2}$$

$$\frac{\partial E^*}{\partial t^*}+\frac{\partial(E^*+p^*)u_j^*}{\partial x_j^*}=\frac{1}{Re}\frac{\partial\left(\tau_{ij}^* u_i^*+\frac{\gamma^*\kappa^*}{Pr}\frac{\partial T^*}{\partial x_j^*}\right)}{\partial x_j^*}+\rho^* f_i^* u_i^*, \tag{3}$$

where all the variables with superscript "$*$" are nondimensionalized by the reference variables (half channel width h, mean bulk density ρ_m, mean bulk velocity U_m, dynamic viscosity at wall μ_w, thermal conductivity at wall κ_w, specific heat at constant volume c_v) in the following way: $x_i^* = x_i/h$, $\rho^* = \rho/\rho_m$, $u_i^* = u_i/U_m$, $E^* = E/(\rho_m U_m^2)$, $p^* = p/(\rho_m U_m^2)$, $\mu^* = \mu/\mu_w$, $\kappa^* = \kappa/\kappa_w$, $T^* = T/(U_m^2/c_v)$, $t^* = t/(h/U_m)$, $f_i^* = f_i/(U_m^2/h)$; where $f_i = \tau_{w_{av}}\delta_{i1}/(h\rho_m)$.

The ideal gas law then becomes,

$$p^* = \rho^*(\gamma-1)T^*. \tag{4}$$

Re is the reference Reynolds number: $Re = \rho_m U_m h/\mu_w$; δ_{ij} is Kronecker's delta: $\delta_{ij} = 1$ if $i = j$; $\delta_{ij} = 0$ if $i \neq j$; τ_{ij}^* is the viscous stress tensor:

$$\tau_{ij}^* = \mu^*\left(\frac{\partial u_i^*}{\partial x_j^*}+\frac{\partial u_j^*}{\partial x_i^*}\right)-\frac{2}{3}\mu^*\delta_{ij}\frac{\partial u_k^*}{\partial x_k^*}; \tag{5}$$

f_i^* is the driving force: $f_i^* = 0.5(\langle\tau_{12}^*\rangle|_{x_2^*=0} - \langle\tau_{12}^*\rangle|_{x_2^*=2})\delta_{i1}/Re$; the angle brackets $\langle\rangle$ denote the average over time (t) and streamwise (x_1) and spanwise (x_3) directions for channel flow; E is the total energy: $E^* = \rho^* T^* + 1/2\rho^* u_i^* u_i^* = p^*/(\gamma-1) + 1/2\rho^* u_i^* u_i^*$.

The relation between the bulk Mach number and the nondimensionalized wall temperature is

$$Ma = \frac{1}{\sqrt{\gamma(\gamma-1)T_w^*}}. \tag{6}$$

Prandtl number is defined as:

$$Pr = \frac{c_p\mu_w}{\kappa_w} = \frac{c_p\mu}{\kappa}. \tag{7}$$

Pr and c_p are constants by assumption. It follows:

$$\kappa^* = \mu^*. \tag{8}$$

The calculation of dynamic viscosity was based on Sutherland's theory of viscosity, for which interpolation formula can be written as [27]:

$$\mu^* = \frac{\mu}{\mu_w} = \left(\frac{T}{T_w}\right)^{\frac{3}{2}}\frac{T_w+S_1}{T+S_1} = \left(\frac{T^*}{T_w^*}\right)^{\frac{3}{2}}\frac{T^*_w+S_1^*}{T^*+S_1^*}, \tag{9}$$

where μ_w denotes the reference dynamics viscosity at the reference wall temperature T_w, S_1 is a constant with a value of $S_1 = 110K$ for air, and $S_1^* = S_1/(U_m^2/c_v)$.

The Navier–Stokes equations (1)–(3) can be rewritten in a compact form as:

$$\mathbf{U}_t + \nabla\cdot\mathbf{F}^I = \frac{1}{Re}\nabla\cdot\mathbf{F}^V + \mathbf{F}_B, \tag{10}$$

where the vector $\mathbf{U} = [\rho^*, \rho^* u^*, \rho^* v^*, \rho^* w^*, E^*]^t$ denotes the conserved variables; $\mathbf{U}_t$ denotes time derivative of the vector $\mathbf{U}$: $\partial\mathbf{U}/\partial t^*$; The inviscid flux $\mathbf{F}^I = \mathbf{F}^I(\mathbf{U})$ and the viscous flux $\mathbf{F}^V = \mathbf{F}^V(\mathbf{U}, \nabla\mathbf{U})$; $\mathbf{F}_B = \left[0, \rho^* f_x^*, \rho^* f_y^*, \rho^* f_z^*, \rho^*\left(f_x^* u^* + f_y^* v^* + f_z^* w^*\right)\right]^t$ represents the body force terms.

The Adams–Bashforth scheme was employed for time integration. DGM was employed for convection and diffusion terms in Eq. (10), but DGM treats these terms differently. The treatment of the convection/inviscid flux term ($\nabla\cdot\mathbf{F}^I$) will be considered first. The contribution of diffusion/viscous fluxes and body force terms will be treated as an correction. The formulation and implementation of DGM discussed in the following are mainly based on the method developed by [14,32].

The convection part of the Eq. (10) is:

$$\mathbf{U}_t + \nabla\cdot\mathbf{F}^I = 0. \tag{11}$$

Let Ω denote the whole computational domain and $\partial\Omega$ the boundary. The whole domain Ω is divided into N subdomains (or elements). $\Omega^e (e = 1, 2, \ldots, N)$ represents the e-th element with boundary $\partial\Omega^e$. Elements are only overlapping on element interfaces. Let $\mathbf{W}$ be the weighting function, which is continuous in Ω^e and zero outside.

DGM treats each element separately. After multiplying the weighting function $\mathbf{W}$ and integrating over the element Ω^e, Eq. (11) becomes,

$$\int_{\Omega^e}\mathbf{W}\mathbf{U}_t d\boldsymbol{x} + \int_{\Omega^e}\mathbf{W}\nabla\cdot\mathbf{F}^I d\boldsymbol{x} = 0. \tag{12}$$

After a series of arrangements, it gives,

$$\int_{\Omega^e}\mathbf{W}\mathbf{U}_t d\boldsymbol{x} + \int_{\Omega^e}\mathbf{W}\nabla\cdot\mathbf{F}^I d\boldsymbol{x} + \int_{\partial\Omega^e}\mathbf{W}\hat{\mathbf{n}}\cdot\left(\widehat{\mathbf{F}}^I - \mathbf{F}^I\right)d\boldsymbol{s} = 0, \tag{13}$$

where the numerical boundary flux $\widehat{\mathbf{F}}^I$ can be written as $\widehat{\mathbf{F}}^I(\mathbf{U}_-, \mathbf{U}_+)$, where $\mathbf{U}_-$ and $\mathbf{U}_+$ are internal and external values of $\mathbf{U}$ at the boundary of element Ω^e. The numerical boundary flux can be computed in many ways such as upwind flux, Roe splitting flux, Lax-Friedriches flux (check [14] for a thorough review). Here upwind flux was employed:

$$\widehat{\mathbf{F}}^I(\mathbf{U}_-, \mathbf{U}_+) = \mathbf{F}^I(\mathbf{R}\mathbf{D}^+\mathbf{L}\mathbf{U}_- + \mathbf{R}\mathbf{D}^-\mathbf{L}\mathbf{U}_+), \tag{14}$$

where $\mathbf{A} = \mathbf{RDL}$ is the Jacobian matrix of $\mathbf{F}^I$;

$$\mathbf{A} = \mathbf{RDL} = \frac{\partial\mathbf{F}^I}{\partial\mathbf{U}}, \tag{15}$$

where $\mathbf{R}$ and $\mathbf{L}$ are its right and left eigenvectors; $\mathbf{D}$ is the diagonal matrix of its eigenvalues and $\mathbf{D}^\pm = \frac{1}{2}(\mathbf{D} \pm |\mathbf{D}|)$.

Similarly, the diffusion part of the Eq. (10) is:

$$\mathbf{U}_t = \frac{1}{Re}\nabla\cdot\mathbf{F}^V + \mathbf{F}_B, \tag{16}$$

where $\mathbf{F}^V = \mathbf{F}^V(\mathbf{U}, \nabla\mathbf{U})$ is the viscous flux.

The treatment of diffusion contribution can be demonstrated by considering the following problem:

$$u_t = \nabla\cdot(v\nabla u) + s, \tag{17}$$

where v is a variable coefficient $v = v(\boldsymbol{x}, t)$; The field variable u is a scalar $u = u(\boldsymbol{x}, t)$; and s is the source term.

A flux variable is introduced:

$$\mathbf{f}^V = v\nabla u. \tag{18}$$

Then the Eq. (17) can be rewritten as:

$$u_t = \nabla\cdot\mathbf{f}^V + s, \tag{19}$$

$$\frac{1}{v}\mathbf{f}^V = \nabla u. \tag{20}$$

Weighting functions $\mathbf{w}$ and v is introduced, so that, for the element Ω^e, it has

$$\int_{\Omega^e} v u_t d\boldsymbol{x} = \int_{\Omega^e} v\nabla\cdot\mathbf{f}^V d\boldsymbol{x} + \int_{\Omega^e} v s d\boldsymbol{x}, \tag{21}$$

$$\int_{\Omega^e} \frac{1}{v}\mathbf{w}\cdot\mathbf{f}^V d\boldsymbol{x} = \int_{\Omega^e} \mathbf{w}\cdot\nabla u d\boldsymbol{x}. \tag{22}$$

After a series of arrangements, it follows:

$$\int_{\Omega^e} v u_t d\boldsymbol{x} = \int_{\Omega^e} v\nabla\cdot\mathbf{f}^V d\boldsymbol{x} + \int_{\Omega^e} v s d\boldsymbol{x} + \int_{\partial\Omega^e} v\hat{\mathbf{n}}\cdot\left(\hat{\mathbf{f}}^V - \mathbf{f}^V\right) d\boldsymbol{s}, \tag{23}$$

$$\int_{\Omega^e} \frac{1}{v}\mathbf{w}\cdot\mathbf{f}^V d\boldsymbol{x} = \int_{\Omega^e} \mathbf{w}\cdot\nabla u d\boldsymbol{x} + \int_{\partial\Omega^e} \mathbf{w}\cdot\hat{\mathbf{n}}(\hat{u} - u) d\boldsymbol{s}, \tag{24}$$

where $\hat{\mathbf{f}}^V$, $\hat{u}$ denotes the numerical viscous boundary fluxes.

There are also many methods available for computing the numerical viscous boundary fluxes, such as, Bassi–Rebay method [3], local discontinuous Galerkin method [7], Baumann–Oden method [4], etc. Here Bassi–Rebay method was employed:

$$\hat{\mathbf{f}}^V = \frac{1}{2}\left(\mathbf{f}^V_+ + \mathbf{f}^V_-\right), \tag{25}$$

$$\hat{u} = \frac{1}{2}(u_+ + u_-). \tag{26}$$

2.2. Physical and numerical parameters

Three DNS cases with Mach numbers $Ma = 0.2$, $Ma = 0.7$, and $Ma = 1.5$ (referred to as Ma02, Ma07, and Ma15 hereafter) based on the bulk velocity U_m are considered. The Reynolds number was ≈ 2800 based on the mean bulk density ρ_m, mean bulk velocity U_m, the dynamic viscosity at wall μ_w and the channel half-width h (180, 186, and 208 based upon the wall shear velocity u_τ and h for $Ma = 0.2$, 0.7, and 1.5, respectively). A summary of the physical parameters of the current simulations and the two reference databases (MKM, CKM) is given in the Table 1. Although there is a slight difference in some of the parameters (such as Reynolds and Prandtl numbers) between the case CKM and the current cases, these differences are minor. The domain size was about the same as MKM and CKM, except in the spanwise direction, where the current domain is about 50% wider. The flow was assumed to be periodic in the streamwise and spanwise directions.

Uniform grid elements were employed in the streamwise and spanwise directions. A hyperbolic tangent function was used to distribute grids in the wall-normal direction. The number of grid elements are $24 \times 15 \times 12$, in x, y, z directions respectively.

The initial field of the current simulations consisted of a uniform density profile ($\langle\rho^*\rangle = 1$), a laminar parabolic velocity profile with a superimposition of random fluctuations ($\langle u^*\rangle = 1.5(1-(1-y^*)^2)$, $\langle v^*\rangle = 0$, $\langle w^*\rangle = 0$), and a total energy profile that makes the mean fluid temperature field uniform ($\langle T^*\rangle = T^*_w$). The simulation started with a polynomial expansion order of $P = 5$th per element and over-integration was applied to avoid aliasing errors; that is, $10 \times 10 \times 10$ quadrature was used in each element; then the simulation was restarted using a $p = 10$th order expansion with over-integration ($20 \times 20 \times 20$ quadrature in each element) to collect the flow statistics. The numerical parameters for the current cases are shown in Table 1 and are based on $p = 10$th order. As noted above, a second-order Adams–Bashforth scheme was used for time discretization. Grid resolutions were fine enough to capture the smallest length scales in the flow, which can be verified by the analysis of Kolmogorov microscales as well as the one dimensional energy spectra and correlations, see [33] for details.

The statistics for all three cases Ma02, Ma07, and Ma15 were obtained by an average over 120 nondimensional time units ($t^* = t/(h/U_m)$), or $\approx 8t/(h/u_\tau)$.

3. Presentation and discussion of results

3.1. Mean profiles of velocity, density and temperature

The mean streamwise velocity, density and temperature profiles for Ma02 and Ma15 are compared with the incompressible case MKM [23] and the compressible case CKM [8] respectively in Fig. 1. The velocity, density and temperature are nondimensionalized by the bulk velocity, bulk density, and the wall temperature, respectively. The wall-normal coordinate y denotes the nondimensionalized variable y/h for convenience. The agreement between the current simulations and those of MKM and CKM is observed to be excellent.

A comparison of the mean density and temperature profiles for Ma02, Ma07 and Ma15 is presented in Fig. 2. It can be seen that the mean density and temperature profiles are sensitive to Mach number. The isothermal wall temperature is lower than the fluid temperature, the maximum of which occurs at the channel center. The larger the Mach number, the higher the temperature gradient close to the wall, and the higher the temperature difference between the wall and the channel center.

The mean velocity profile for the Ma02 case was generated and it is in good agreement with the incompressible case of MKM. However, both cases do not collapse onto the log-law, which is due to the low Reynolds number effect, as discussed in [23].

Wall bounded flows maybe plotted using the traditional log-law or a power law:

$$u^+ = a(y^+)^b, \tag{27}$$

Table 1
Physical and numerical parameters.

Case	Ma	Re	Re_τ	Pr	L_x	L_y	L_z	Δx^+	$\Delta y^+_{min}/\Delta y^+_{max}$	Δz^+
MKM	0	2800	178	–	$4\pi h$	$2h$	$\frac{4}{3}\pi h$	17.7	0.1/4.4	5.9
CKM	1.5	3000	222	0.7	$4\pi h$	$2h$	$\frac{4}{3}\pi h$	19	0.1/5.9	12
Ma02	0.2	2772	180	0.72	$12h$	$2h$	$6h$	4.74	0.19/2.81	4.74
Ma07	0.7	2795	186	0.72	$12h$	$2h$	$6h$	4.89	0.19/2.89	4.89
Ma15	1.5	2811	208	0.72	$12h$	$2h$	$6h$	5.42	0.22/3.24	5.42

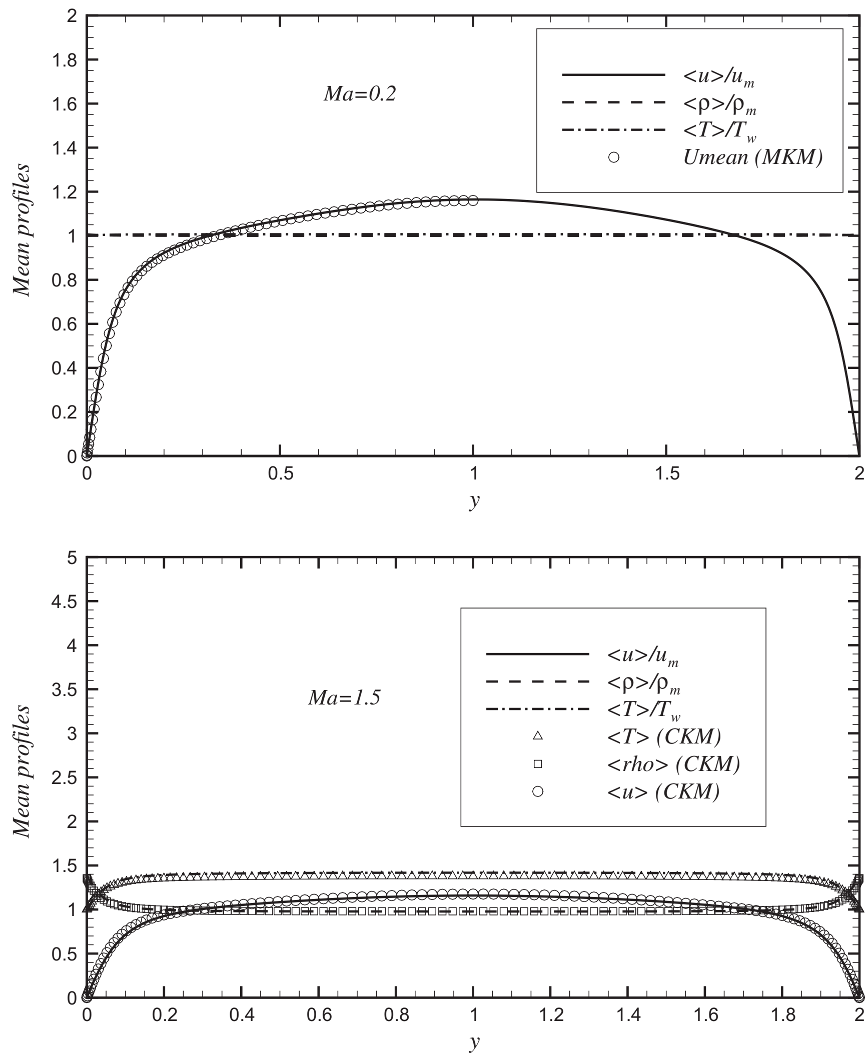

Fig. 1. Mean streamwise velocity, density and temperature profiles for the case Ma02 and Ma15 versus the case MKM [23] and CKM [8] respectively.

which has been proposed by, for example, George and Castillo [11] and Barenblatt et al. [2]. Barenblatt and coworkers claimed a power law for the intermediate region of both boundary layer and wall-bounded flows; however, George and coworkers suggested that a power law was only applicable for boundary layers and the log-law should be used for wall-bounded flows like channel and pipe flows [35,23]. The scientific discussion arising from new observations from pipe, channel, and boundary layer flows, reinforce the uncertainty as to what best describes these flows [18]. Note, too, that here, $Re_\tau \approx 200$ and that the effects of viscosity outside the viscous sublayer ought to be better captured by a power law, rather than a log-law, the appearance of which requires $Re_\tau > \mathcal{O}(1000)$, see for example Zagarola et al. [37], Morrison et al. [22].

The power and log-laws are considered here to ascertain their performance when applied to compressible flows and to determine their dependence on Mach number. Two quantities are often used to compare the performance of power law and log-law to decide which one is more suitable for the scaling. They are defined as follows [23]:

$$\beta = \frac{y^+}{u^+}\frac{du^+}{dy^+}, \tag{28}$$

$$\gamma = y^+\frac{du^+}{dy^+}. \tag{29}$$

$\beta$is supposed to be a constant (that is, b in Eq. (27)) in the region where a power law applies. γ should be $1/\kappa$ in the region where log-law applies. β and γ for Ma02, Ma07, and Ma15 are shown in Fig. 3. It can be seen that the power law displays a more consistent variation with y^+ than the log-law, and remains constant over a wider region, say, $50 < y^+ < 150$ (i.e. overlap region). Moser et al. [23] performed a similar study for the scaling of mean velocities with Reynolds number and found that neither the power law nor the log-law was obeyed exactly although β increased more slowly with y^+ than γ for the high Reynolds number cases. Similarly, the data in the figure suggests that the power law seems to be better than the log-law for the scaling of the mean streamwise velocity with Mach number.

The mean pressure, nondimensionalized by the wall pressure, is presented in Fig. 4. It is observed that the position of the minimum pressure shifts from $y \approx 0.3$ for the case Ma02 to $y \approx 0.4$ for the case Ma15, which is the same as the shift of positions of the maximum root-mean-square wall-normal velocity fluctuations, as will be discussed in the next section. The value of the minimum pressure decreases with increasing Mach number.

3.2. Second-order statistics

The root-mean-square (RMS) profiles for Ma02 match almost perfectly with the incompressible case MKM [23]. The RMS profiles for Ma15 match well with the CKM case [8]. The inner scaling of

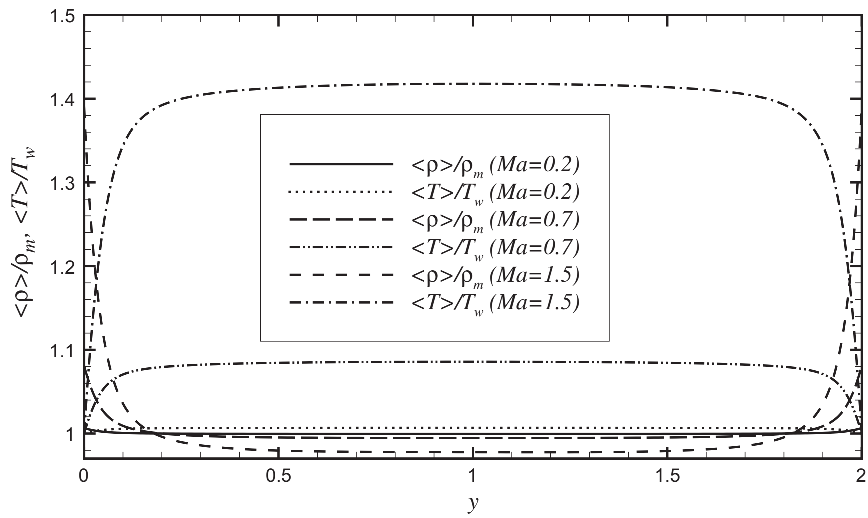

Fig. 2. Profiles of mean density normalized by the bulk density and the mean temperature normalized by wall temperature (right) for the cases Ma02, Ma07, and Ma15 in global coordinates.

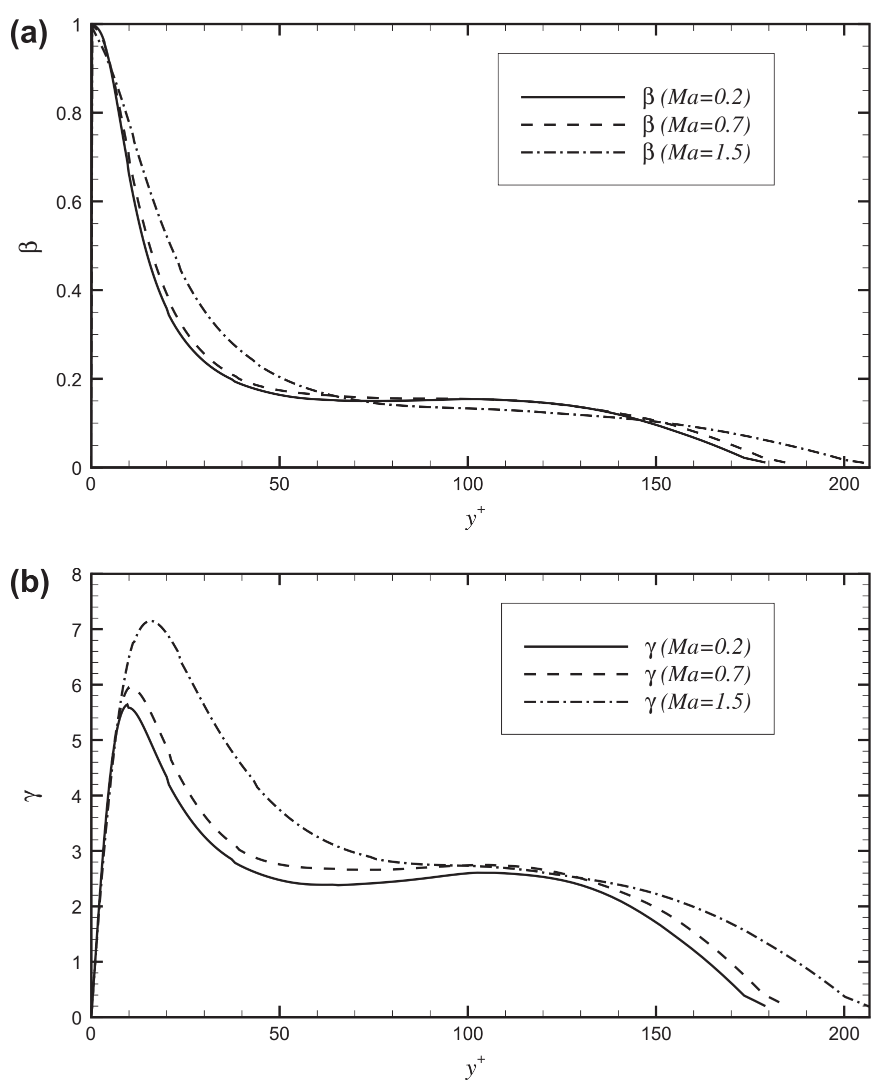

Fig. 3. (a) A power law quantity (β) for Ma02, Ma07, and Ma15 in wall coordinates. (b) A log-law quantity (γ) for Ma02, Ma07, and Ma15 in wall coordinates.

the RMS velocity fluctuations (normalized by the wall variables u_τ, ν/u_τ) shows that the maximum is increased and its location is shifted away from the wall, with increasing Mach number. Similar trends are observed for the RMS wall-normal and spanwise velocity fluctuations. The outer scaling (normalized by global variables u_m, h) shows a good collapse in the region around $y > 0.5$ for all components of RMS velocity fluctuations. Details can be found at [33].

The current cases consider a single Reynolds number but different Mach numbers and, as will be shown later, the Mach number does affect the large-scale motions near the wall. It is possible that this effect causes an inner scaling dependence with Mach number, which in some sense agrees with Morrison's arguments about the influence of large-scale motions [22,21].

The RMS density and temperature fluctuations normalized by local mean density $\langle\rho\rangle$ and local mean temperature $\langle T\rangle$ respectively for Ma02, Ma07, and Ma15 are illustrated in Fig. 5 (top) in wall units. RMS density and temperature fluctuations share a similar trend, including the location of their maxima $y^+ \approx 10$. The maximum turbulence kinetic energy production usually occurs at $y^+ \approx 15$, which can also be seen in the turbulence kinetic energy budget section, see Section 3.4. It is interesting to see that the Prandtl number ($Pr = 0.72$) corresponds approximately to the ratio of these two values. There is a slight shift in y^+ of the maximum position in these quantities with Mach number. The shift is not as significant as that associated with the RMS velocity fluctuations; however, the maximum value of RMS density and temperature increases more significantly with increasing Mach number.

Fig. 5 (bottom) displays the RMS density and temperature fluctuations normalized by the mean bulk density ρ_m and the mean bulk velocity square over specific heat at constant volume U_m^2/c_v respectively scaled in global coordinates. The results show a better collapse in the region $y \geqslant 0.5$ than the top figure.

The agreement between the present distribution of the RMS vorticity fluctuations, normalized by the mean shear at the wall τ_w/μ_w for Ma02, with data from the incompressible case of MKM is good, see Wei [33]. The collapse of the wall-parallel components of the RMS vorticity fluctuations $(\omega_x)_{rms}$ (streamwise) and $(\omega_z)_{rms}$ (spanwise) is a little better than the collapse of the RMS wall-normal vorticity fluctuation $(\omega_y)_{rms}$, in the region around $y^+ \approx 25$; although all three components of RMS vorticity fluctuations for the case Ma02 are slightly smaller than the case MKM. We attribute these minor differences to improved grid resolution in the current simulations.

Among the three components of the RMS vorticity fluctuations, the wall-normal component is the only one that is independent of Reynolds number when scaled using wall variables for incompressible channel flows [1,23]. For compressible flows, the RMS wall-normal and total vorticity fluctuations become smaller in the near-wall region with increase of Mach number when inner scaling is used, as shown in Fig. 19 of Coleman et al. [8].

Three components of the RMS vorticity fluctuations, normalized by τ_w/μ_w, are compared in Fig. 6 in wall coordinates. The figure shows that $(\omega_x)_{rms}$ and $(\omega_z)_{rms}$ in the near-wall region $y^+ < 30$ decreases with increase in the Mach number. The local minimum of $(\omega_x)_{rms}$ close to the wall changes from $y^+ \approx 5$ for $Ma = 0.2$ to $y^+ \approx 7$ for $Ma = 1.5$. The local maximum of $(\omega_x)_{rms}$ shifts from $y^+ \approx 20$ for $Ma = 0.2$ to $y^+ \approx 36$ for $Ma = 1.5$. As the local maximum of $(\omega_x)_{rms}$ denotes the averaged center of the streamwise vortices and local minimum correspond to the averaged edge of the vortex [24,15], Fig. 6 indicates that the averaged streamwise eddy size increases with increase in the Mach number, but its strength decreases with increasing Mach number. In other words, near-wall large-scale motions are affected by Mach number. It is interesting to note that all components roughly collapse onto one line in the region $y^+ > 80$, which indicates in this region, Mach number effects are minimal.

The RMS pressure fluctuations normalized by $\rho_w u_\tau^2$ and $\rho_m U_m^2$ in wall and global coordinates respectively are presented in Fig. 7. The top figure shows that with increase of Mach number the RMS pressure fluctuations decrease in the region close to the wall, but increase in the region close to the center of the channel, and the position of the maximum shifts away from the wall. Outer variable scaling, shown in the bottom figure, indicates high sensitivity to Mach number.

Decomposition of the shear stresses and several different forms of turbulence stresses ($\langle\rho\rangle\langle u'v'\rangle$, $\langle\rho\, u'v'\rangle$, $\langle\rho\rangle\langle u''v''\rangle$, where $''$ denotes fluctuations based on Favre average, defined as $\{\phi\} = \langle\rho\ \phi\rangle/\langle\rho\rangle$) normalized by the wall shear stress τ_w for Ma02 indicates excellent agreement with MKM, Wei [33]. The turbulence stresses, calculated according to Reynolds and Favre-type averaging, display little difference for Ma02 and Ma07. For Ma15, however, the profile of $\langle\rho u'v'\rangle$ is slightly higher than $\langle\rho\rangle\langle u'v'\rangle$ in the region where the maximum turbulence stress is located. Almost no difference between $\langle\rho\rangle\langle u'v'\rangle$ and $\langle\rho\rangle\langle u''v''\rangle$ is observed for the current cases, as one would probably expect, particularly for $Ma < 1$.

The comparison of the turbulence and viscous shear stresses is illustrated in Fig. 8 in wall coordinates. The increase of turbulence

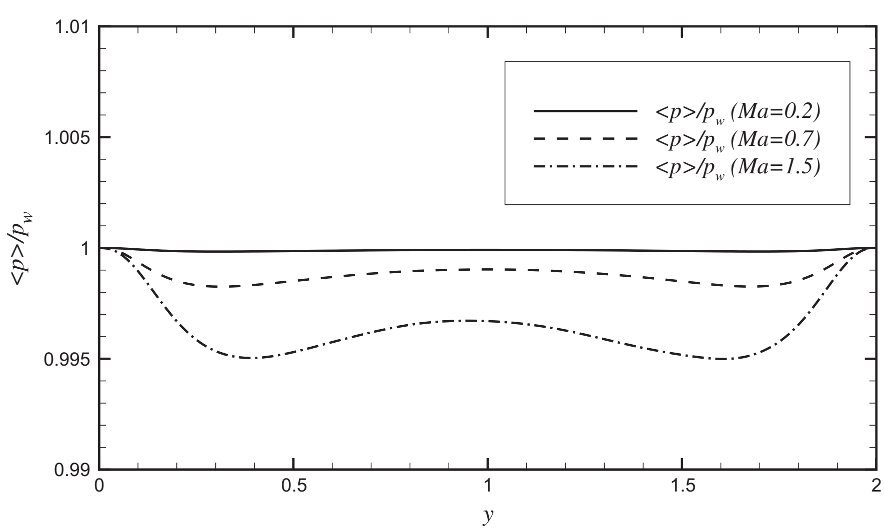

Fig. 4. Mean pressure profile for the cases Ma02, Ma07, and Ma15.

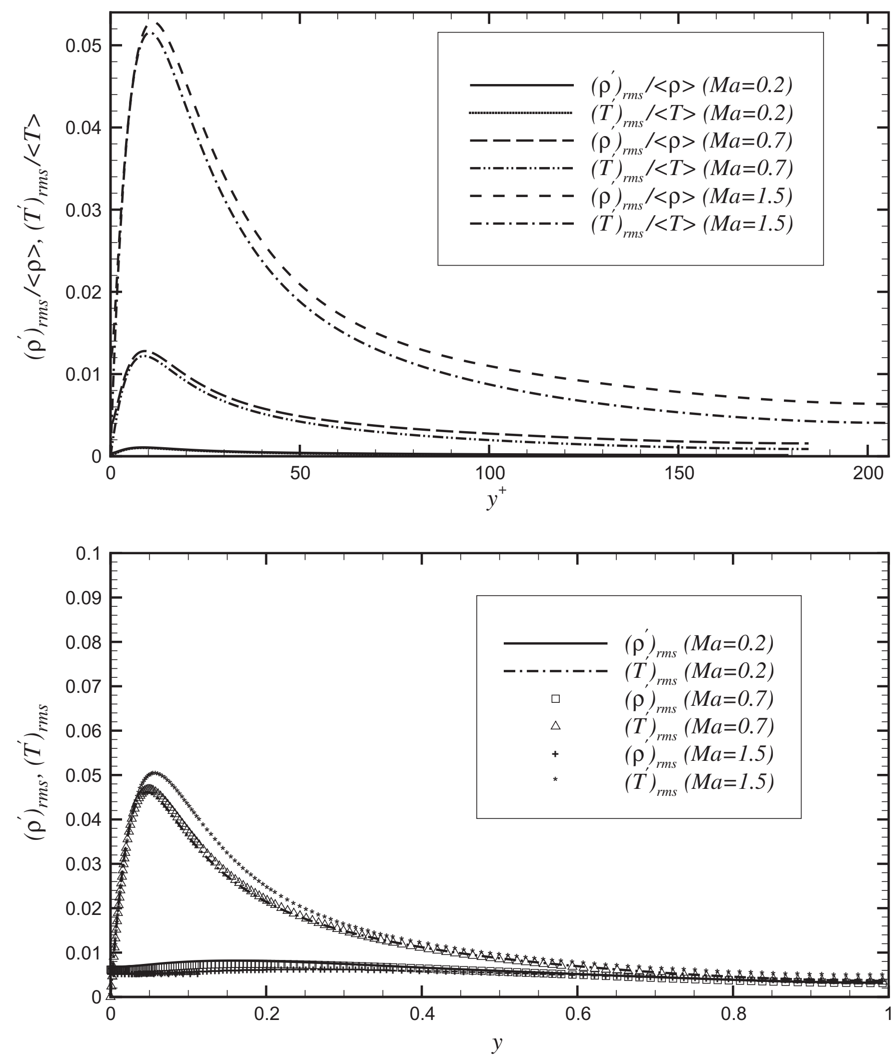

Fig. 5. Top: RMS density and temperature fluctuations normalized by local mean density $\langle\rho\rangle$ and local mean temperature $\langle T\rangle$ respectively in wall coordinates. Bottom: RMS density and temperature fluctuations normalized by the mean bulk density ρ_m and the mean bulk velocity square over specific heat at constant volume U_m^2/c_v respectively in global coordinates.

stress with Mach number is limited to approximately $y^+ < 70$. In wall coordinates, Mach number influences on the turbulence stresses is evident.

3.3. Higher-order statistics

Higher-order statistics considered here are the skewness and kurtosis (flatness) factors. The skewness (S) and flatness (F) factors of, for example, the velocity fluctuation u', are defined as:

$$S(u') = \frac{\langle (u')^3 \rangle}{\langle u'u' \rangle^{3/2}} = \frac{\langle (u - \langle u \rangle)^3 \rangle}{\langle (u - \langle u \rangle)^2 \rangle^{3/2}}, \tag{30}$$

$$F(u') = \frac{\langle (u')^4 \rangle}{\langle u'u' \rangle^{2}} = \frac{\langle (u - \langle u \rangle)^4 \rangle}{\langle (u - \langle u \rangle)^2 \rangle^{2}}, \tag{31}$$

where $\langle\rangle$ denotes an average over time t and x, z directions.

The calculation of higher-order statistics usually requires more data than that acquired to calculate the second-order statistics. As indicated in Kim et al. [15], oscillations and asymmetry in the skewness and flatness profiles suggest that the sample size used for the computation may not be adequate, and the skewness of spanwise velocity $S(w')$ should be zero due to the reflection symmetry of the solutions of Navier–Stokes equations. In other words, the oscillation, symmetry, and $S(w')$ may be used as the indicators of the quality of the statistics. Note, too, that the skewness statistics normally converge more slowly than those for flatness.

The skewness and flatness factors for velocity and pressure fluctuations for the case Ma02 in wall coordinates, compared with the case MKM, is given in Fig. 9. As can be seen from Fig. 9, there are few oscillations observed and the skewness of w' is essentially zero for Ma02. Although there seems to be a big difference in the sample size used here for the case Ma02 and those of MKM, the collapse of the profiles of $S(u')$ is good for almost the whole region, and $S(v')$ collapses well except for a small region close to the wall ($y^+ < 15$). In other words, when compared with $S(v')$, $S(w')$, and $S(p')$, $S(u')$ is less affected by the sample size. The figure also shows that the sample size has a great effect on $S(p')$.

The general agreement between the current simulations and those for MKM for the skewness is good. It is shown that flatness factors of velocities collapse in the central region of the channel ($y^+ > 50$); that is, it displays an almost Gaussian distribution. Flatness of pressure $F(p')$ is much larger than that of velocities in this region, which indicates that pressure fluctuations are more intermittent.

The skewness of velocities and pressure fluctuations for the cases Ma02, Ma07, and Ma15 are compared in Fig. 10 in wall coor-

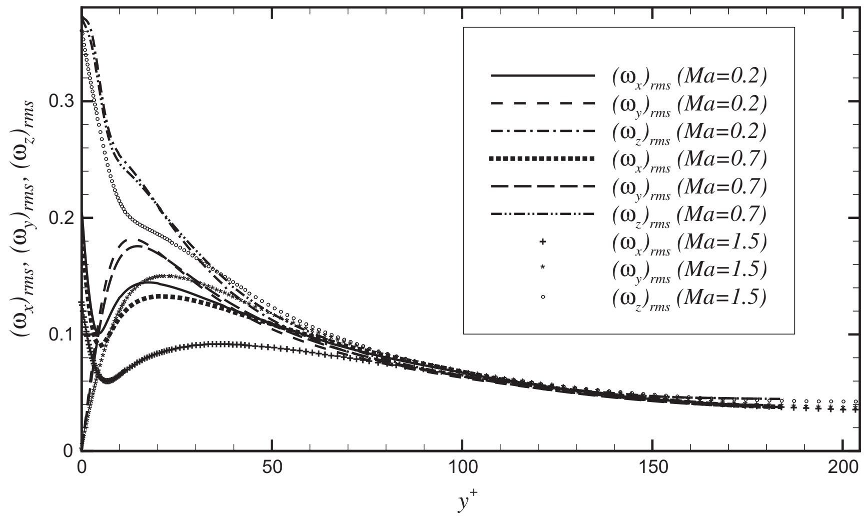

Fig. 6. RMS vorticity fluctuations normalized by the mean shear at the wall τ_w/μ_w for Ma02, Ma07, and Ma15 in wall coordinates.

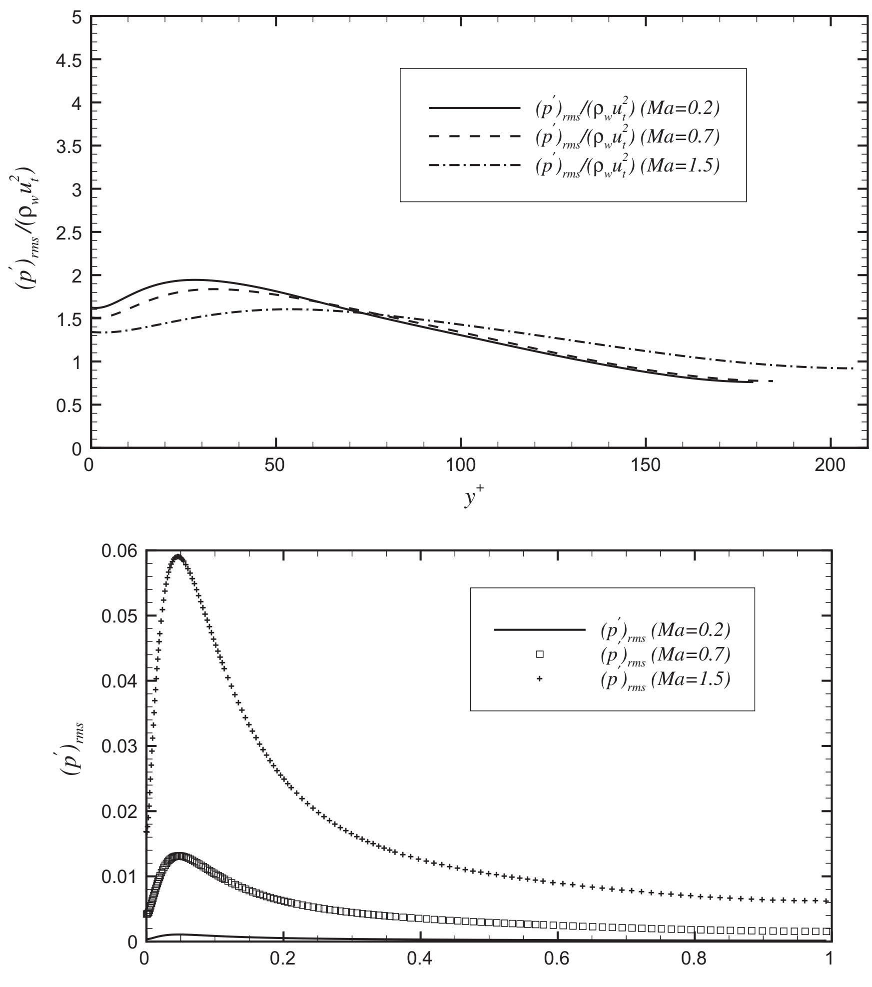

Fig. 7. Top: RMS pressure fluctuations normalized by the wall shear stress $\rho_w u_\tau^2$ for Ma02, Ma07, and Ma15 in wall coordinates. Bottom: RMS pressure fluctuations normalized by the mean bulk quantity $\rho_m U_m^2$ for Ma02, Ma07, and Ma15 in global coordinates.

dinates. Generally speaking, the influence of Mach number on the profiles is not significant in the current Mach number range ($0.2 < Ma < 1.5$).

The skewness of density and temperature fluctuations are given in Fig. 11. The profile of the skewness of temperature $S(T')$ is similar to $S(u')$ but with a lower magnitude. This can be explained by

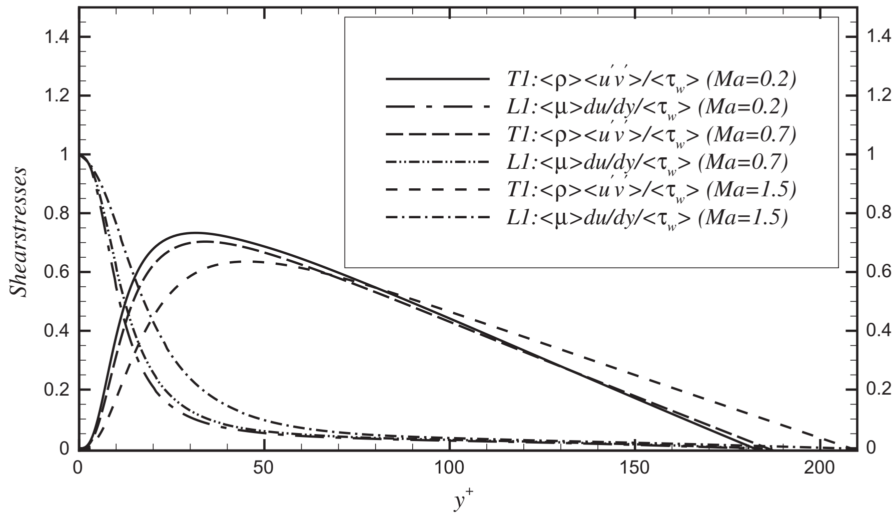

Fig. 8. Turbulence and viscous shear stresses normalized by the wall shear stress τ_w Shear stresses for all three cases Ma02, Ma07, and Ma15 in wall coordinates.

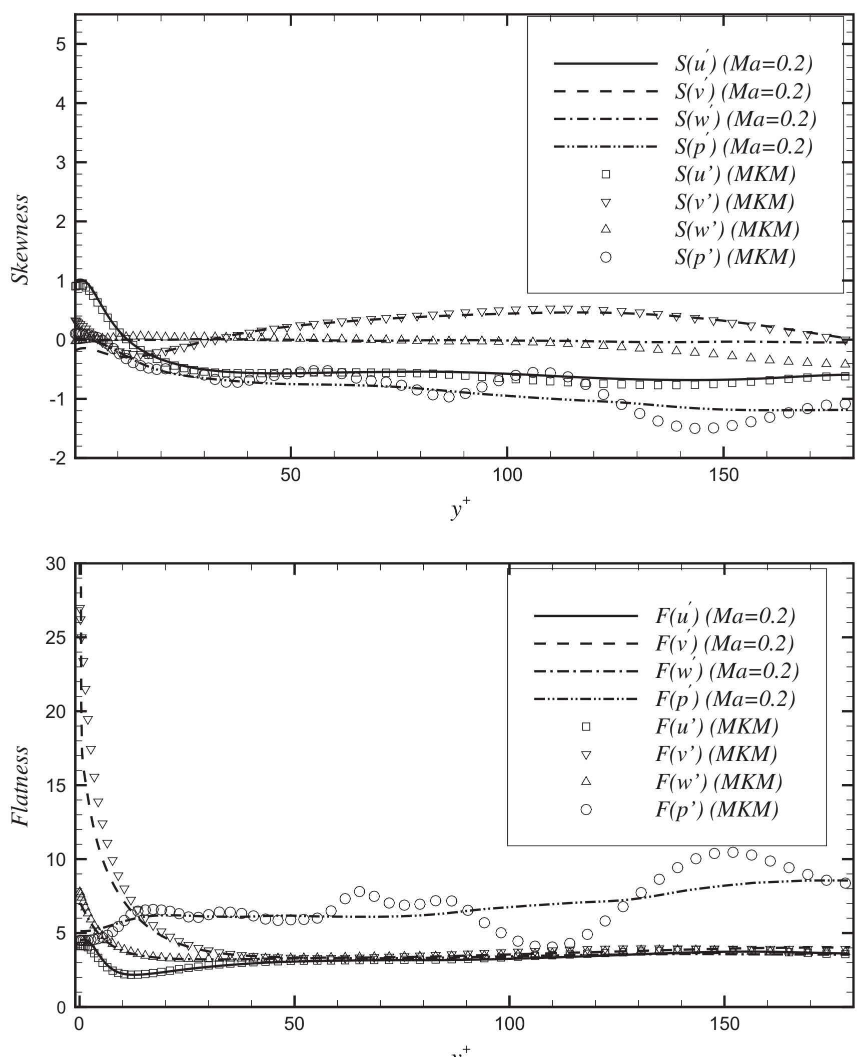

Fig. 9. Skewness (top) and flatness (bottom) factors of velocity and pressure fluctuations for the case Ma02 in wall coordinates versus the case MKM.

the high correlations between velocity and temperature, as will be discussed in the next section. It is noted that close to the wall, Ma number effects on $S(\rho')$ and $S(T')$ are negligible. It is also interesting to note that the location of the local minimum of $S(\rho')$ close to the wall and the local maximum of $S(\rho')$ is similar to the RMS streamwise vorticity fluctuation $(\omega_x)_{rms}$ shown in Fig. 6.

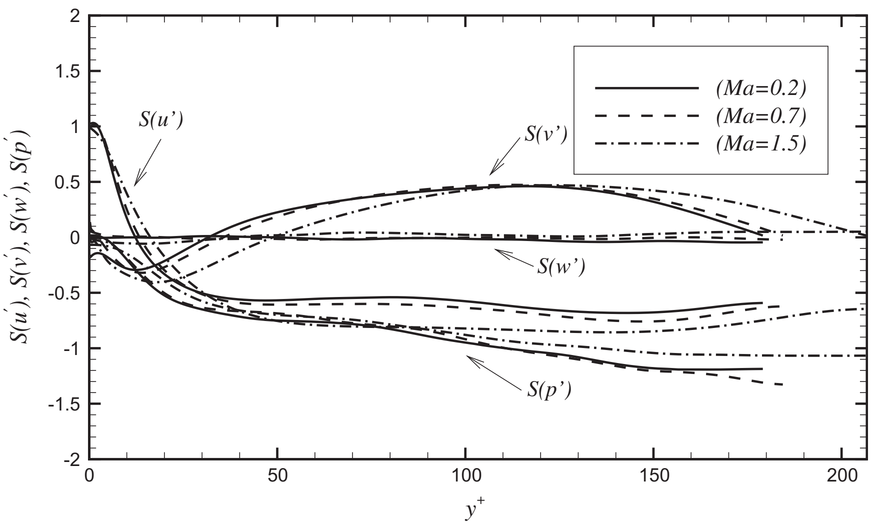

Fig. 10. Skewness factors of velocity and pressure fluctuations for all three cases in wall coordinates.

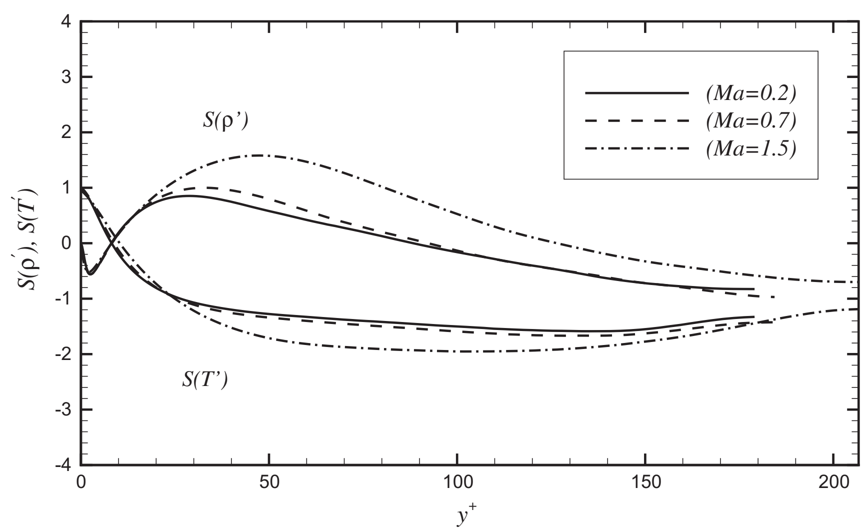

Fig. 11. Skewness factors of density and temperature fluctuations for all three cases in wall coordinates.

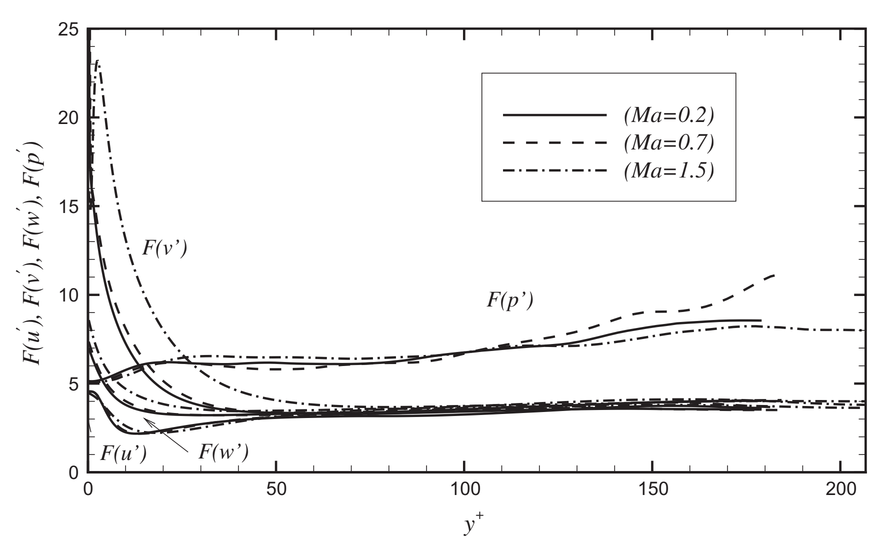

Fig. 12. Flatness factors of velocity and pressure fluctuations for all three cases in wall coordinates. Note the diminution in $F(v')$ for $y^+ < 3$ for the case $Ma = 1.5$.

The effect of Mach number on the scaling of the flatness factors of velocity, pressure fluctuations is displayed in Fig. 12. It seems that $F(u')$ and $F(p')$ are not affected significantly by Mach number, whereas the profile of $F(v')$ near the wall for the case Ma15 behaves differently. The $F(v')$ profile for Ma15 first increases until $y^+ \approx 2.6$ and then drops suddenly as it moves from the center of the channel to the wall, an effect also observed by [30]. They argued that it was due to the low Reynolds number and the effects of compressibility. As this phenomenon is not observed for the cases Ma02 and Ma07, it is suggested here that it is possibly due to effects of high gradients in the near-wall viscosity.

The flatness factors of density and temperature fluctuations are illustrated in Figs. 13. The flatness of density $F(\rho')$ and temperature $F(T')$ show similar trends. The scaling with Mach number is very good close to the wall. The higher value in the central region of the channel indicates highly intermittent fluctuations.

3.4. Turbulent kinetic energy budget

The turbulent kinetic energy (TKE, $k = 0.5\langle\rho\rangle\{u_i''u_i''\}$) equation for compressible flows can be written as [13]:

$$\frac{\partial \frac{1}{2}\langle\rho\rangle\{u_i''u_i''\}\{u_j\}}{\partial x_j} = -\langle\rho\rangle\left\{u_i''u_j''\right\}\frac{\partial\{u_i\}}{\partial x_j} - \frac{\partial\left(\frac{1}{2}\langle\rho\rangle\left\{u_i''u_i''u_j''\right\} - \left\langle u_i'\tau_{ij}'\right\rangle + \left\langle u_j'p'\right\rangle\right)}{\partial x_j} - \left\langle\tau_{ij}'\frac{\partial u_i'}{\partial x_j}\right\rangle - \langle u_i''\rangle\frac{\partial\langle p\rangle\delta_{ij}}{\partial x_j} + \langle u_i''\rangle\frac{\partial\langle\tau_{ij}\rangle}{\partial x_j} + \left\langle p'\frac{\partial u_j'}{\partial x_j}\right\rangle. \tag{32}$$

This form is a little different from the traditional Favre-averaged TKE equation [16,12] as the Favre-averaging process was only used on the convective terms in the compressible Navier–Stokes equations. However, this form of the TKE equation is equivalent to the traditional (Reynolds averaged) TKE form, as the different terms $\partial\left\langle u_i'\tau_{ij}'\right\rangle/\partial x_j$, $\partial\left\langle u_j'p'\right\rangle/\partial x_j$, $\left\langle p'\partial u_j'/\partial x_j\right\rangle$, $\left\langle\tau_{ij}'\partial u_i'/\partial x_j\right\rangle$ in Eq. (32) are equal to the respective terms of the traditional form: $\partial\left\langle u_i''\tau_{ij}'\right\rangle/\partial x_j$, $\partial\left\langle u_j''p'\right\rangle/\partial x_j$, $\left\langle p'\partial u_j''/\partial x_j\right\rangle$, $\left\langle\tau_{ij}'\partial u_i''/\partial x_j\right\rangle$, as $\langle a'b'\rangle = \langle a'b''\rangle$.

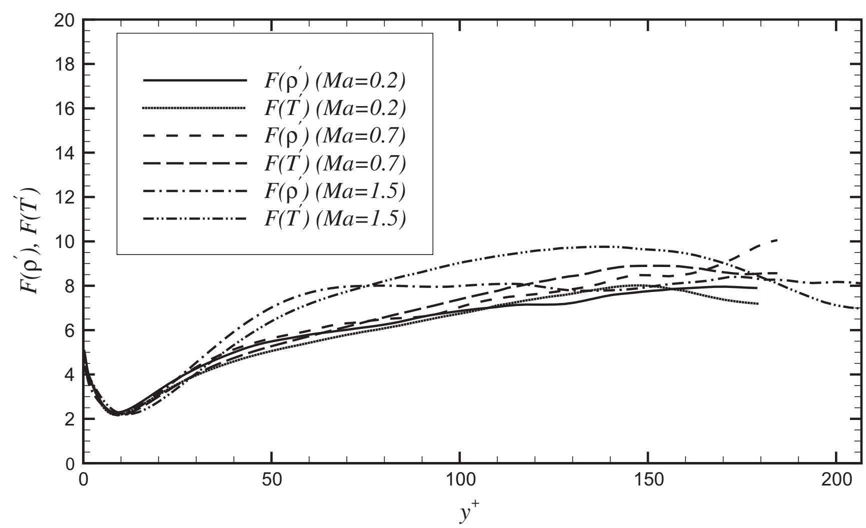

Fig. 13. Flatness factors of density and temperature fluctuations, in wall coordinates.

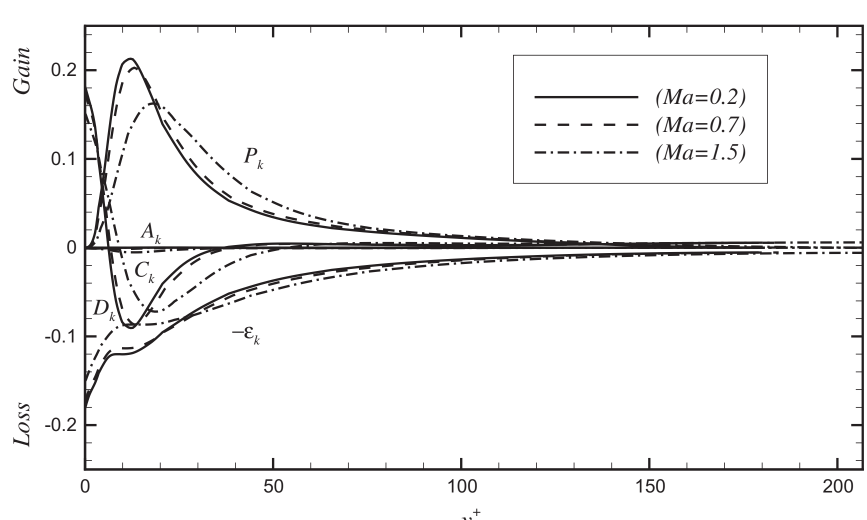

Fig. 14. Turbulent kinetic energy budget normalized by wall variables $\tau_w u_\tau/\delta_v$ in wall coordinates.

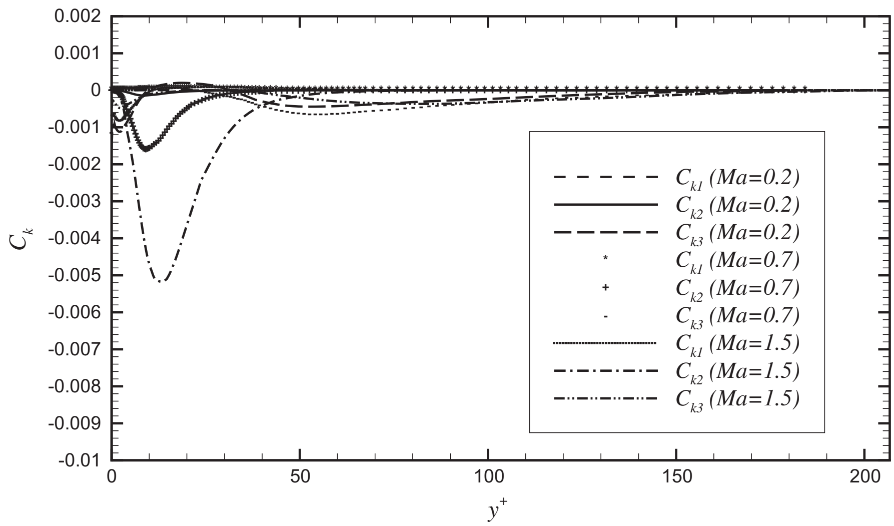

Fig. 15. Compressibility terms of TKE equation (Eq. (38)) normalized by wall variables $\tau_w u_\tau / \delta_v$ in wall coordinates.

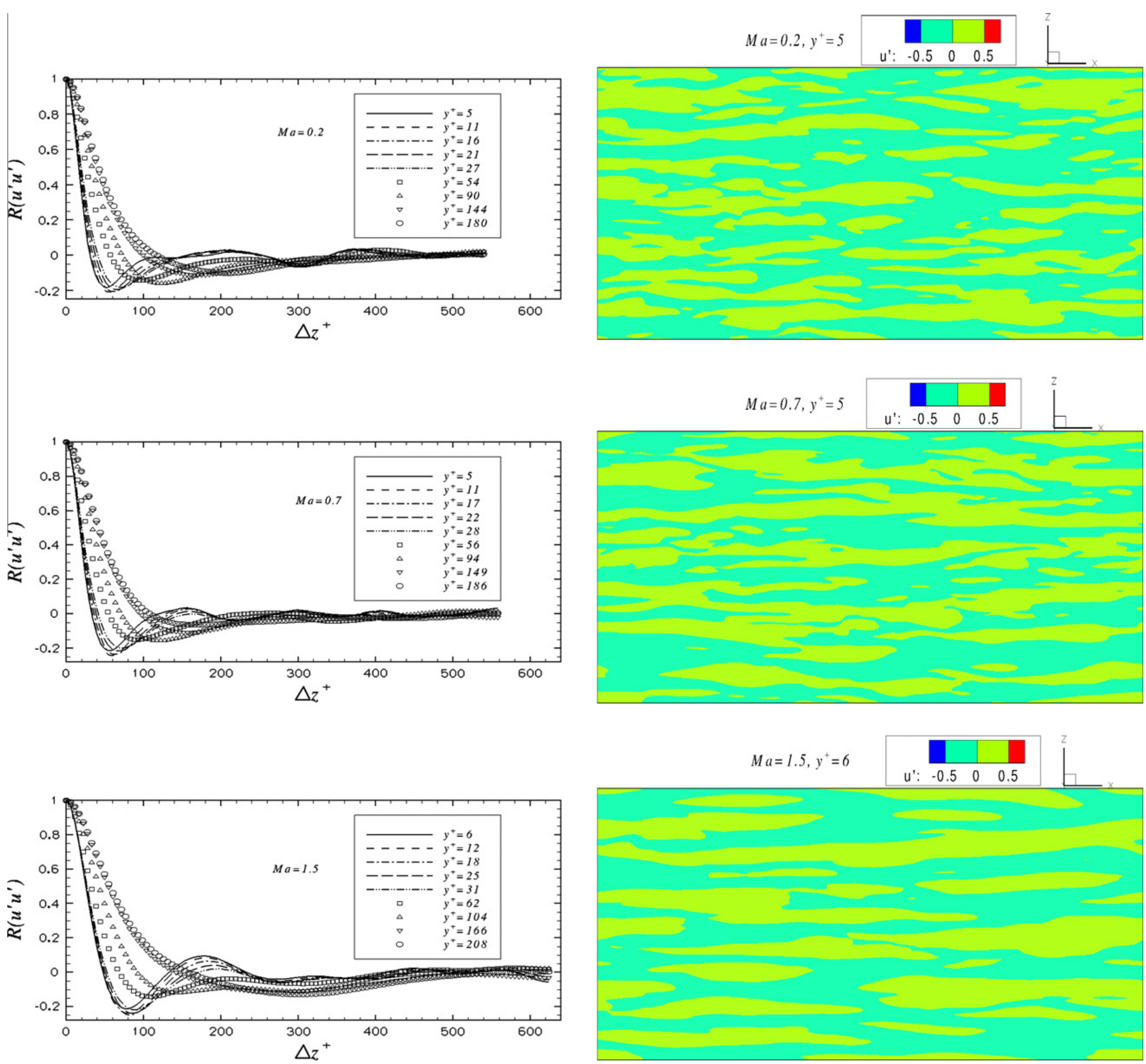

Fig. 16. Left Column: Correlations of streamwise velocity fluctuations at different y locations for the cases Ma02 (top), Ma07 (middle) and Ma15 (bottom). Right Column: A snapshot of streamwise velocity fluctuations at $y = 0.03$ ($y^+ \approx 5$) for the case Ma02 (top), Ma07 (middle), and Ma15 (bottom) respectively.

The streamwise (x_1) and spanwise (x_3) directions may be averaged so that Eq. (32) can be simplified to,

$$A_k = P_k + D_k + \epsilon_k + C_k; \tag{33}$$

Where the terms in the TKE Eq. (33) are denoted as,

Advection:

$$A_k = \frac{\partial \frac{1}{2} \langle \rho \rangle \{u_i'' u_i''\} \{u_2\}}{\partial x_2}; \tag{34}$$

Production:

$$P_k = -\langle \rho \rangle \{u_i'' u_2''\} \frac{\partial \{u_i\}}{\partial x_2}; \tag{35}$$

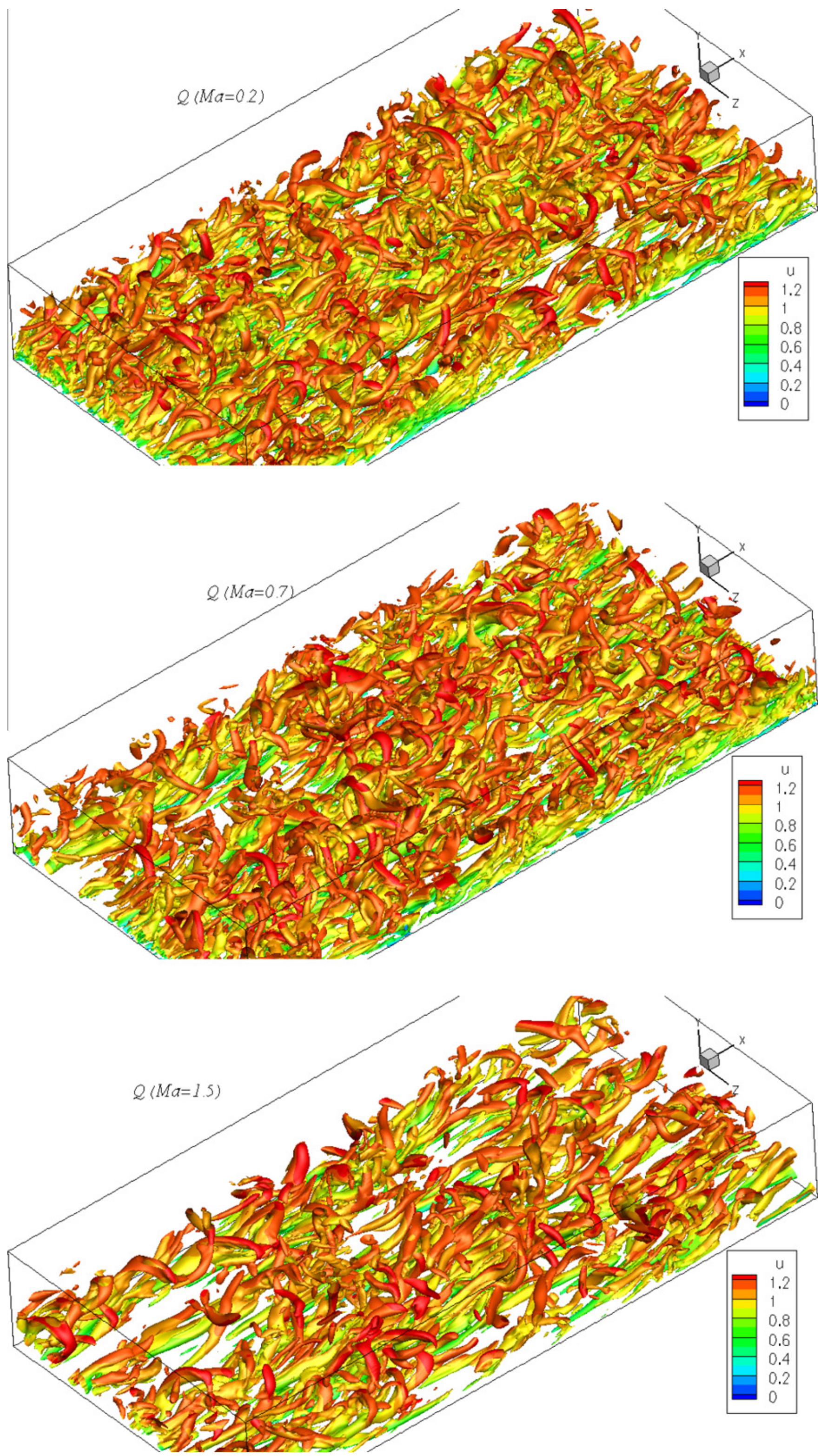

Fig. 17. Iso-surfaces of second invariant of the velocity gradient tensor ($Q = 0.5$) in the bottom half channel (structures in the top half channel are removed for clarity) for Ma02, Ma07 and Ma15. The coloring is based on the local streamwise velocity.

Diffusion:

$$D_k = -\frac{\partial\left(\frac{1}{2}\langle\rho\rangle\{u_i''u_i''u_2''\} - \langle u_i'\tau_{i2}'\rangle + \langle u_2'p'\rangle\right)}{\partial x_2}; \tag{36}$$

Dissipation:

$$\epsilon_k = \left\langle \tau_{ij}''\frac{\partial u_i'}{\partial x_j}\right\rangle; \tag{37}$$

Compressibility:

$$C_k = -C_{k1} + C_{k2} + C_{k3}, \tag{38}$$

where $C_{k1} = \langle u_2''\rangle\partial\langle p\rangle/\partial x_2,\ C_{k2} = \langle u_i''\rangle\partial\langle\tau_{i2}\rangle/\partial x_2,\ C_{k3} = \left\langle p'\partial u_j'/\partial x_j\right\rangle$ is the pressure-dilatation correlation term.

The TKE budget normalized by wall variables $\tau_w u_\tau/\delta_v$ (viscous length scale $\delta_v = v/u_\tau$) for all three cases Ma02, Ma07, and Ma15 is given in the top of the Fig. 14. The advection terms should be and are zero for all cases. The maximum turbulence production decreases with increasing Ma number and with distance from the wall. A similar trend is observed for the turbulence dissipation and diffusion terms. On the contrary, the magnitude of compressibility terms increase as Mach number increases. However, the influence of compressibility terms is small and mainly contained in the near-wall region. Further discussion of compressibility terms will be dealt with shortly. It can also be seen that there is an obvious Ma number effect in the near-wall region.

We now return to compressibility effects. Fig. 15 provides a plot for the three compressibility terms: C_{k1}, C_{k2}, C_{k3} for three Mach numbers where inner scaling is used, as was presented for the term C_k in Fig. 14. It shows that the compressibility term C_k in the TKE equation is mainly affected by the term C_{k2}. This was addressed by Morinishi et al. [19]. The magnitude of the term C_{k2} increases significantly near the wall and its maximum moves farther away from the wall, as the Mach number increases.

3.5. Near-wall turbulence structures

Near-wall streaks, which are characteristic of wall-bounded turbulent flows [26], are referred to as narrow regions of near-wall low speed fluid stretched in the streamwise direction [28]. [28] studied characteristics of near-wall streaks in a turbulent boundary layer for a Reynolds number range of $740 < Re_\theta < 5830$ and found that the near-wall low speed streaks had a mean spanwise spacing of $\Delta z^+ \approx 100$ in wall units, which was independent of Reynolds number; however, the spanwise streak spacing was found to increase with increasing distance from the wall. Numerical results of Kim et al. [15] confirmed these findings by considering spanwise autocorrelations of streamwise velocity fluctuations. Morinishi et al. [19] reported that the spanwise streak spacing is around 100 in semi-local wall units $(\delta_{v^*} = \langle\mu\rangle/(\langle\rho\rangle u_{\tau^*}), u_{\tau^*} = (\tau_w/\langle\rho\rangle)^{0.5})$ for compressible channel flow.

The spanwise correlations of streamwise velocities at different y locations for all three cases Ma02, Ma07, and Ma15 are given in Fig. 16 in wall units. It can be seen that the location of the minimum of the correlations increases as the distance from the wall increases for all cases. The minimum is significant in the near-wall region ($y^+ < 30$). Comparison for three cases shows that the location of the minimum of the correlation in the near-wall region increases as Mach number increases, which corresponds to increased streak spacing. It is found that the near-wall low speed streak spacings (twice of the location Δz^+ of minimum correlation of streamwise velocity fluctuations) for the case $Ma = 0.2$ increases from around 100 wall units at $y^+ \approx 5$ to around 140 at $y^+ \approx 27$, which agrees well with the incompressible experimental and numerical results reported by Kim et al. [15], Smith and Metzler [28]. It is also found that the spacing at $y^+ \approx 5$ increases from around 100 wall units for the case $Ma = 0.2$ to around 150 for the case $Ma = 1.5$.

The visualization of the streaks is also indicated in Fig. 16, which is taken from a snapshot of streamwise velocity fluctuations at $y/h = 0.03$ ($y^+ \approx 5$) for the case Ma02 (top), Ma07 (middle), and Ma15 (bottom) respectively. The streaks lengthen in the streamwise direction and become wider in the spanwise direction as the Mach number increases. In other words, the mean spanwise streak spacing increases with increasing Mach number, which confirms the previous predictions based on spanwise correlations of streamwise velocities. Additional discussion of near-wall streaks of density, temperature, vorticity and their interactions can be found in Wei and Pollard [34].

The second invariant of the velocity gradient tensor (denoted as Q) is usually used for the visualization of turbulent coherent structures. It is defined as [5]

$$Q = \frac{1}{2}(P^2 - S_{ij}S_{ji} - R_{ij}R_{ji}), \tag{39}$$

where $P = -\partial u_i/\partial x_i$ is zero for incompressible flows, $S_{ij} = 0.5(\partial u_i/\partial x_j + \partial u_j/\partial x_i)$, and $R_{ij} = 0.5(\partial u_i/\partial x_j - \partial u_j/\partial x_i)$.

Iso-surfaces of $Q = 0.5$ (nondimensionalized by bulk velocity and half channel width) in the bottom half channel (structures in the top half channel are removed for clarity) for the cases Ma02, Ma07, and Ma15 are presented in Fig. 17. The coloring of the iso-surfaces is based on the local streamwise velocity, which is similar to Wu and Moin [36]. It can be seen here that the structures are more sparsely distributed and elongated as Mach number increases, which is similar to the distribution of near-wall low speed streaks. The inclined hairpin-like structures with both one leg and two legs are observed, but only a few have two legs with heads, *i.e.* a full hairpin structure.

4. Concluding remarks

DNS of fully developed, isothermal wall, turbulent channel flow at Mach numbers $Ma = 0.2$, $Ma = 0.7$, and $Ma = 1.5$ and Reynolds number $Re \approx 2800$ has been performed. The agreement between the current simulation results obtained using DGM and the corresponding incompressible DNS data of MKM and compressible DNS data of CKM is satisfactory, thereby demonstrating the utility of the DGM for DNS.

Compared with the log-law, a power law seems to slightly better represent the scaling of mean streamwise velocity with Mach number for the current cases, although the mean velocity profiles of the current cases do not exactly obey power law either all of which is likely the effects of the low Reynolds number used in the simulations.

Second-order and higher-order statistics scalings have been discussed. It is found that the inner scaling of second-order statistics, such as velocity, density, temperature, shear stress and vorticity fluctuations, is dependent of Mach number; but outer scaling with Mach number (i.e. density, temperature fluctuations) shows a better collapse. Near-wall large-scale motions are affected by Mach number.

The TKE budget has been reported. The related scaling and analysis of compressibility terms have been analyzed. The result shows that the inner scaling of TKE budget does not collapse well in the near-wall region. The influence of compressibility terms on the TKE budget is negligible.

Near-wall streaks, indicated by the spanwise correlation of streamwise velocity fluctuations and by the snapshot of streamwise velocity fluctuations close to the wall, have been analyzed. The agreement of spanwise streak spacing between the case Ma02 and the incompressible data [15] is good. The spanwise streak spacing, while it is generally known to be independent of Reynolds numbers, increases with increasing Mach number and this was confirmed by the snapshot of near-wall streak contours. Iso-surfaces of second invariant of the velocity gradient tensor are more sparsely distributed and elongated as Mach number increases, which is similar to the distribution of near-wall low speed streaks.

Acknowledgements

The authors would like to thank Dr. George Karniadakis and his CRUNCH group and Dr. Mike Kirby for providing the original discontinuous Galerkin code and the related helpful email discussions. We also thank Dr. Robert Moser and Dr. Gary N. Coleman for the use of their DNS data. The research was funded through grants from NSERC Canada. Computing resources were provided by HPCVL (www.hpcvl.org).

References

[1] Antonia RA, Kim J. Low-Reynolds-number effects on near-wall turbulence. J Fluid Mech 1994;276:61–80.
[2] Barenblatt GI, Chorin AJ, Prostokishin VM. Scaling laws for fully developed turbulent flow in pipes. Appl Mech Rev 1997;50:413–29.
[3] Bassi F, Rebay S. A high-order accurate discontinuous finite element method for numerical solution of the compressible Navier–Stokes equations. J Comput Phys 1997;131:267–79.
[4] Baumann CE, Oden JT. A discontinuous hp finite element method for convection-diffusion problems. Comput Methods Appl Mech Eng 1999;175:311–41.
[5] Chong MS, Perry AE, Cantwell BJ. A general classification of three dimensional flow fields. Phys Fluids A 1990;2(5):765–77.
[6] Cockburn B, Karniadakis G, Shu C-W. Discontinuous Galerkin methods – theory, computation and applications. Springer; 2000.
[7] Cockburn B, Shu C-W. The local discontinuous Galerkin method for time-dependent convection diffusion problems. SIAM J Numer Anal 1998;35:2440–63.
[8] Coleman GN, Kim J, Moser RD. A numerical study of turbulent supersonic isothermal-wall channel flow. J Fluid Mech 1995;305:159–83.
[9] Collis SS. Discontinuous Galerkin methods for turbulence simulation. In: Proceedings of the summer program. California, USA: Center for Turbulence Research; 2002.
[10] Foysi H, Sarkar S, Friedrich R. Compressibility effects and turbulence scalings in supersonic channel flow. J Fluid Mech 2004;509:207–16.
[11] George WK, Castillo L. Zero-pressure-gradient turbulent boundary layer. Appl Mech Rev 1997;50:689–729.
[12] Guarini SE, Moser RD, Shariff K, Wray A. Direct numerical simulation of a supersonic turbulent boundary layer at Mach 2.5. J Fluid Mech 2000;414:1–33.
[13] Huang P, Coleman G, Bradshaw P. Compressible turbulent channel flows: DNS results and modelling. J Fluid Mech 1995;305:185–218.
[14] Karniadakis G, Sherwin S. Spectral/hp element methods for computational fluid dynamics. 2nd ed. Oxford Science Publications; 2005.
[15] Kim J, Moin P, Moser R. Turbulence statistics in fully-developed channel flow at low Reynolds number. J Fluid Mech 1987;177:133–66.
[16] Lele SK. Compressibility effects on turbulence. Annu Rev Fluid Mech 1994;26:211–54.
[17] Moin P, Mahesh K. Direct numerical simulation: a tool in turbulence research. Annu Rev Fluid Mech 1998;30:539–78.
[18] Monty JP, Hutchins N, Ng HCH, Marusic I, Chong MS. A comparison of turbulent pipe, channel and boundary layer flows. J Fluid Mech 2009;631:431–42.
[19] Morinishi Y, Tamano S, Nakabayashi K. Direct numerical simulation of compressible turbulent channel flow between adiabatic and isothermal walls. J Fluid Mech 2004;502:273–308.
[20] Morkovin MV. Effects of compressibility on turbulent flows. In: Favre A, editor. The mechanics of turbulence. New York: Gordon and Breach; 1964. p. 367–80.
[21] Morrison JF. The interaction between inner and outer regions of turbulent wall-bounded flow. Phil Trans Roy Soc London Ser A 2007;365:683–98.
[22] Morrison JF, McKeon BJ, Jiang W, Smits AJ. Scaling of the streamwise velocity component in turbulent pipe flow. J Fluid Mech 2004;508:99–131.
[23] Moser RD, Kim J, Mansour NN. Direct numerical simulation of turbulent channel flow up to $re_\tau \approx 590$. Phys Fluids 1999;11(4):943–5.
[24] Moser RD, Moin P. Direct numerical simulation of curved turbulent channel flow. Tech. rep., NASA TM 85794, Department of Mechanical Engineering, Stanford University, Stanford, California, USA; 1984.
[25] Reed W, Hill T. Triangular mesh methods for the neutron transport equation. In: LA-UR 479. Los Alamos, USA: Springer; 1973.
[26] Robinson SK. Coherent motions in the turbulent boundary layer. Annu Rev Fluid Mech 1991;23:601–39.
[27] Schlichting H. Boundary-layer theory. 7th ed. McGraw-Hill Book Company; 1979.
[28] Smith CR, Metzler SP. The characteristics of low-speed streaks in the near-wall region of a turbulent boundary layer. J Fluid Mech 1983;129:27–54.
[29] Smits A. Turbulent boundary-layer structure in supersonic flow. Phil Trans Roy Soc London Ser A 1991;336:81–93.
[30] Tamano S, Morinishi Y. Effect of different thermal wall boundary conditions on compressible turbulent channel flow at $m = 1.5$. J Fluid Mech 2006;548:361–73.
[31] Van Driest ER. Turbulent boundary layer structure in compressible fluids. J Aero Sci 1951;18:145–60.
[32] Warburton TC, Karniadakis GE. A discontinuous Galerkin method for the viscous MHD equations. J Comput Phys 1999;152:608–41.
[33] Wei L. Direct numerical simulation of compressible and incompressible wall bounded turbulent flows with pressure gradients. Ph.D. thesis, Queen's University, Kingston, Ontario, Canada; 2009.
[34] Wei L, Pollard A. Interactions among pressure, density, vorticity and their gradients in compressible turbulent channel flows. J Fluid Mech; in press. doi:10.1017/S0022112010006166.
[35] Wosnik M, Castillo L, George WK. A theory for turbulent pipe and channel flows. J Fluid Mech 2000;421:115–45.
[36] Wu X, Moin P. Direct numerical simulation of turbulence in a nominally zero-pressure-gradient flat-plate boundary layer. J Fluid Mech 2009;630:5–41.
[37] Zagarola MV, Perry AE, Smits AJ. Log laws or power laws: the scaling in the overlap region. Phys Fluids 1997;9(7):2094–100.